

# Density evolution of a copper wire during nanosecond timescale underwater explosions

M. Nitishinskiy,<sup>1</sup> A. Virozub,<sup>1</sup> A. Rososhek,<sup>1</sup> D. Yanuka,<sup>2</sup> and Ya. E. Krasik<sup>1</sup>

<sup>1</sup>Physics Department, Technion, Haifa 32000, Israel

<sup>2</sup>Plasma Physics Group, Imperial College London, London SW7 2BW, United Kingdom

(Received 9 July 2018; accepted 7 September 2018; published online 28 September 2018)

We present high-contrast X-ray images ( $\sim 30 \mu\text{m}$  space and  $\sim 10 \text{ ns}$  time resolution) of ns-timescale underwater electrical explosions of copper wires to the low density limit of  $\sim 1 \text{ g/cm}^3$ , using a rod-ring electron diode as a source of X-rays. The radial density distribution, obtained by inverse Abel transform analysis of the X-ray images, is reproduced by one dimensional magneto-hydrodynamic (MHD) simulations using the SESAME equations of state and a modified Bakulin, Kuropatenko, and Luchinskii conductivity model for copper. These modifications are introduced by matching the experimental and simulated current and voltage waveforms and the radial wire expansion. For our ns-timescale copper wire underwater electrical explosions, the X-ray images display no MHD and thermal instabilities. *Published by AIP Publishing.* <https://doi.org/10.1063/1.5047566>

## I. INTRODUCTION

Underwater electrical wire explosions<sup>1–9</sup> (UEWE) on timescales of  $10^{-7}$ – $10^{-6}$  s and current densities above  $10^7 \text{ A/cm}^2$  are accompanied by fast solid-liquid-vapour-plasma phase transitions and can be applied in the study of Warm Dense Matter<sup>10</sup> (WDM) in laboratory conditions. Such studies allow one to confirm the validity of the Equations of State<sup>11</sup> (EOS) and the conductivity models<sup>12–16</sup> of different materials in a broad range of pressures, densities, and temperatures. In contrast to wire explosions in vacuum or gas, the high electric field breakdown threshold in water ( $>200 \text{ kV/cm}$ ) prevents surface plasma channel formation, which in addition to small water compressibility results in a relatively slow ( $\leq 3 \times 10^5 \text{ cm/s}$ ) radial expansion of the exploding wire. These advantages of UEWE allow one to sustain high energy density deposition into the wire during the entire period of the overdamped discharge and deposit almost the entire initially stored energy.

We model UEWE by self-consistently solving the magneto-hydrodynamic (MHD) equations coupled to Ohm's law, the electrical circuit equation, the Wiedemann–Franz law, EOS and the conductivity model.<sup>3,4,17–25</sup> Simulations show a complex time- and space evolution of the exploding wire parameters (pressure, density, temperature, and resistivity) which depend on the rate of energy density deposition, wire dimensions, and material properties. Moreover, these simulations show the possible co-existence of the various phases, fast growing thermal instabilities, and anomalous fast magnetic field diffusion.

In experiments of UEWE, the discharge current and voltage are measured. The acquired data, which take into account the inductive voltage, are used to calculate the energy deposition rate into the exploding wire. Framing and streak laser-backlit shadow imaging with  $\sim 10^{-3} \text{ cm}$  space and  $\sim 10^{-8}$  s time resolution are applied to measure the radial expansion of the exploding wire and follow the generated shock wave.<sup>26–28</sup> The waveforms of the discharge current, the resistive voltage,

and the radial expansion of the exploding wire are then compared with the results of numerical simulations. If the experimental data and the numerical results do not agree, the EOS and the conductivity models are modified accordingly.<sup>8,20–22,28</sup> However, even when satisfactory agreement is achieved, the question of uniqueness of the fitting procedure remains unanswered, since the pressure, temperature, density, internal energy, and conductivity are interdependent values. It is impossible to measure the time-dependent current density or the radial distribution of the thermodynamic parameters during the wire explosion using the laser-backlit shadow imaging technique. Instead, X-ray imaging or GeV-scale energy proton-beam-radiography<sup>29</sup> can be used to measure the time-dependent radial density distribution of the exploding wire. For proton radiography, the spatial resolution strongly depends on the quality of the proton beam and its reproducibility. Synchrotron produced X-ray ( $\sim 30 \text{ keV}$ ) radiation with the time and space resolution of  $\sim 10^{-9}$  s and  $\sim 10^{-3} \text{ cm}$ , respectively,<sup>30</sup> is very promising, but the use of a large synchrotron facility is very costly.

For wire explosions in vacuum or gas, X-pinch is used as a sub-nanosecond and very bright point-like soft X-ray source.<sup>31,32</sup> However, this method is not applicable to UEWE because photon energies exceeding  $30 \text{ keV}$  are needed due to the absorption in the water and the windows. This obstacle can be overcome by using hybrid X-pinch which produce intense  $\sim 10^{-8}$  s long hard X-ray fluxes generated in plasma filled micro-diodes,<sup>33</sup> with an image spatial resolution of  $20 \mu\text{m}$ . However, this approach requires a high-current ( $>100 \text{ kA}$ ) pulse power nanosecond (ns) timescale generator. Recently, the X-ray flux generated in a compact vacuum diode by the application of a High-Voltage (HV) ns-timescale pulse was successfully applied to obtain X-ray images of UEWE on the microsecond timescale.<sup>34,35</sup> The radial density distributions with a space resolution of  $\sim 50 \mu\text{m}$  of an exploding Cu wire obtained by the inverse Abel transform of X-ray images were in good agreement with the results of MHD simulations, validating the

SESAME EOS<sup>11</sup> for copper and the Bakulin, Kuropatenko, and Luchinskii (BKL) conductivity model<sup>12</sup> used in these simulations.

In this paper, we present first experimental results on X-ray imaging with an improved space resolution of  $\sim 30 \mu\text{m}$  of ns-timescale underwater electrical explosion of Cu wires using a modified X-ray generator with increased X-ray flux compared to that used in our previous work on microsecond timescale UEWE.<sup>35</sup> The X-ray images were analyzed using the inverse Abel transform, and the experimental radial distributions of the exploding wire were compared with the results of one dimension (1D) MHD modeling.

## II. EXPERIMENTAL SETUP AND DIAGNOSTICS

The experimental setup is shown in Fig. 1. In experiments, we used a high-current generator<sup>19</sup> delivering a negative polarity of 110 kV, 80 ns pulse to the matched load of  $1.5 \Omega$ .

The output of the spark gap switch (see Fig. 1) was connected through an interface insulator to the inner HV electrode (10 mm diameter) of the short water-filled coaxial line (23.5 cm long and 2.6 cm inner diameter). A 45 mm long and  $130 \mu\text{m}$  diameter copper wire was stretched coaxially inside a Delrin tube between two end cap electrodes connected to the HV and the grounded electrodes. The tube had two longitudinal slots on opposite sides. Two windows for X-ray imaging were made in the outer electrode, at the axial position corresponding to the middle of the wire. These windows, 12 mm diameter each, were fitted with 2 mm thick Perspex plates. The total inductance and capacitance of the coaxial line including the load were  $\sim 63 \text{ nH}$  and  $\sim 1.1 \text{ nF}$ , respectively. Two calibrated self-integrated Rogowski coils were used to measure the waveforms of the input and output currents (see Fig. 1). Current losses in the water line were measured to be  $\leq 5 \text{ kA}$ . The voltage was measured by a capacitive voltage divider and corrected to inductive voltage  $[-Ldi(t)/dt]$ . The inductance  $L$  was determined in shots of the HV generator with a short-circuit load.

In these experiments, a vacuum rod-ring electron diode,<sup>36</sup> supplied by a HV pulse ( $\sim 160 \text{ kV}$ ,  $\sim 1.6 \text{ kA}$ , and  $\sim 10 \text{ ns}$ ) produced by an 18 stage low inductance Marx generator, was used to generate an intense X-ray flux. The diode design was modelled using a ray tracing software.<sup>37</sup> The vacuum

( $< 30 \text{ mPa}$ ) diode (see Fig. 2) consists of a HV 3 mm diameter W tip of a conical ( $30^\circ$ ) anode and a 1-mm thick graphite ring anode with an inner diameter of 2 mm with a  $45^\circ$  sharp edge slope. The cathode holder allows precise coaxial adjustment of the ring relative to the anode tip. Preliminary shots with different anode-cathode axial gaps showed that the maximal X-ray flux without shorting the anode-cathode gap by explosive emission cathode plasma was  $\sim 1.5 \text{ mm}$ . The modeling showed that the main X-ray flux is generated from a less than  $0.1 \text{ mm}$  diameter part of the anode cone tip.

In our earlier research,<sup>35</sup> we used the electron emission from the surface of the explosive emission plasma formed at the tip of a conical W cathode. These electrons accelerate towards a conical W anode in the presence of a guiding external magnetic field. Only a small part of the generated X-rays, which are directed perpendicularly to the axis of the diode, take part in the X-ray imaging. The design used here (Fig. 2) generates a significantly higher ( $\sim 7$  times) X-ray flux in the region of the investigated object. An X-ray flux generated by the electrons at the tip of the anode was radiated through a 5 mm-thick Perspex window inserted in the front flange of the chamber. The X-ray energy spectrum was determined using two Hamamatsu R 7400U Photo-Multiplier Tubes (PMT) with a 2-mm EJ-200 scintillator. One PMT was used as a reference and the other was covered by Ni filters with varying thicknesses of 40, 80, 140, 220, 320, and  $500 \mu\text{m}$ . The experimentally obtained X-ray flux attenuation curve was compared with the attenuation of the X-ray flux with the energy spectrum simulated with the *SPEKTR* software<sup>38</sup> (see Fig. 3) with a maximum at  $\sim 45 \text{ keV}$  in the photon energy distribution.

This novel X-ray diode design allowed us to decrease the distance between the anode of the x-ray source and the

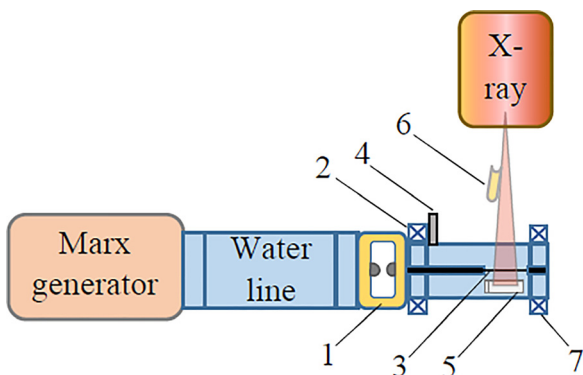


FIG. 1. Experimental setup. (1) Spark gas switch; (2) Rogowski coil; (3) copper wire; (4) capacitive voltage divider; (5) X-ray film; (6) PMT; (7) Rogowski coil.

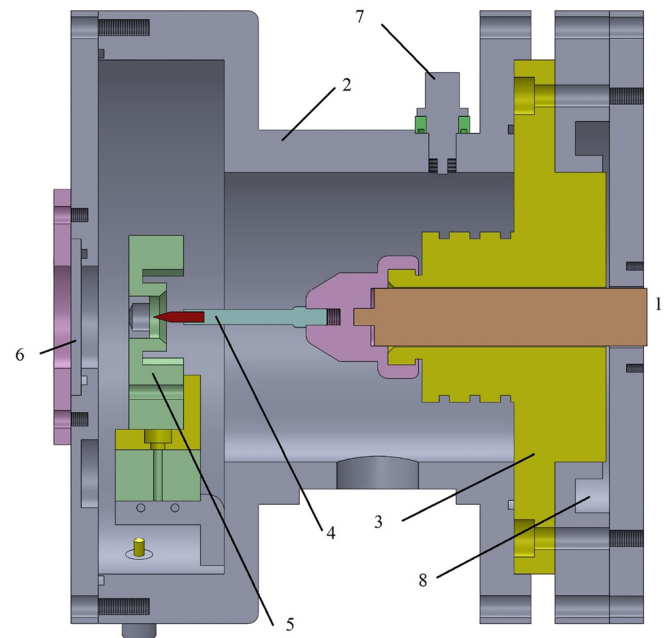


FIG. 2. Cross sectional mechanical drawing of the X-ray diode: 1—HV input from the Marx generator; 2—vacuum chamber; 3—insulator; 4— anode holder and anode; 5—cathode holder and cathode; 6—output window; 7—output of the voltage divider; 8—Rogowski coil (not shown).

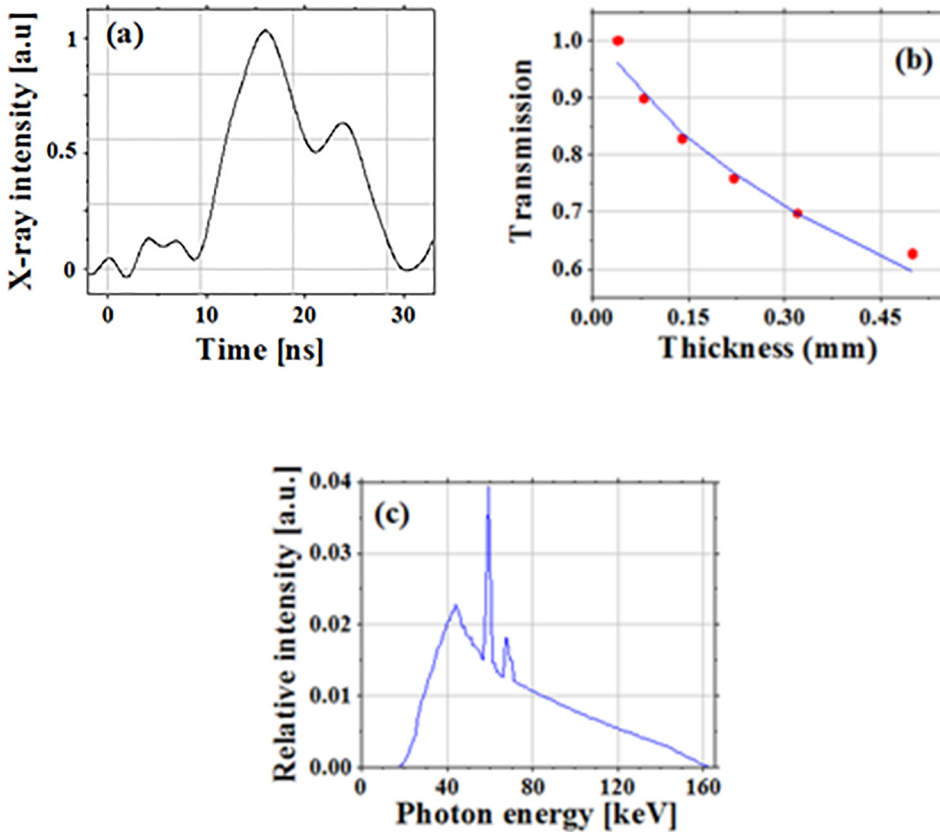


FIG. 3. (a) Time dependent X-ray flux intensity and (b) attenuation of X-rays by the Ni filters. Dots—experimental data; line—attenuation of simulated X-ray spectrum shown in (c).

exploding wire from  $\sim 200$  mm used previously<sup>35</sup> to 130 mm. The PMT was used to monitor the X-ray flux for each shot of the generator (see Fig. 1). The signals from the Rogowski coils, the voltage divider, and the PMT were registered by a Tektronix 2024B digital oscilloscope. For a timed firing of the ns-time scale generator and the Marx generator used for charging the X-ray diode, we used a digital delay generator BNC 575 producing TTL signals with variable time delays. However, because of a relatively large total time jitter ( $\pm 30$  ns), the time delay between the beginning of the discharge current and the maximum in the intensity of the X-ray flux was measured using the waveforms of the discharge current and the scintillator luminescence obtained by the output Rogowski coil and the PMT, respectively (see Fig. 1).

In our earlier research,<sup>35</sup> an X-ray image of the exploding wire was obtained using a CMOS sensor placed 90 mm from the object. The latter results in a spatial resolution of  $\sim 50$   $\mu\text{m}$  in the radial direction. In this research, dental films (*Carestream E-speed*) placed behind the wire at a distance of 6 mm were used to take X-ray images of the exploding wire. This allowed us to obtain a space resolution of  $\sim 30$   $\mu\text{m}$  limited by the grain size of the film. After the exposure, the film was developed and scanned with a resolution of 4800 ppi. The optical density of the images corresponds to the linear part of the characteristic curve of the film, i.e., the scanned intensity values are proportional to the X-ray exposure.

### III. MHD MODELING

The main purpose of this research was to determine the time and space resolved radial density distributions of the exploding wire and comparison of these distributions with

those obtained by 1D MHD modeling. The correctness of this modeling was verified by fitting the simulated current, the voltage waveforms, and the radial expansion of the wire, with the corresponding experimentally obtained values. This modeling, which accounts for thermal diffusion and is coupled with the electrical circuit equation, the EOS<sup>11</sup> for copper and water and the conductivity model,<sup>12</sup> was described in detail in earlier publications.<sup>19,20</sup> Similar to the results presented in Ref. 20, the application of the original BKL conductivity model does not result in agreement with the experimental data. Thus, in order to obtain a satisfactory fit, the conductivity values in the BKL model<sup>12</sup> were modified. An example for these modifications for three different

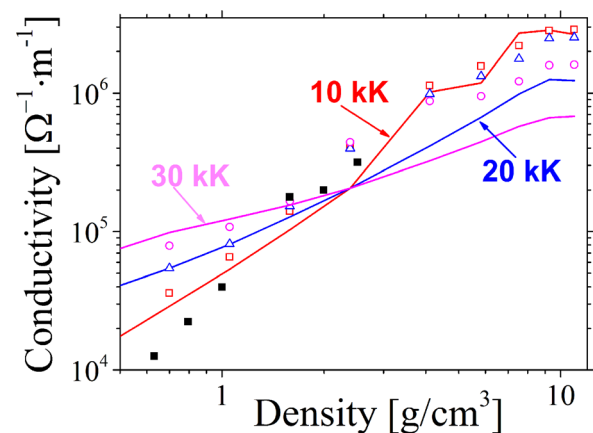


FIG. 4. Electrical conductivity of the copper plasma. Lines—BKL<sup>12</sup> model for 10, 20, and 30 kK. Color symbols—modified BKL, used in the present research: red square—10 kK, blue triangle—20 kK, and pink circle—30 kK. Black dots—conductivity values measured by DeSilva and Katsouris<sup>3</sup> for 10 kK.

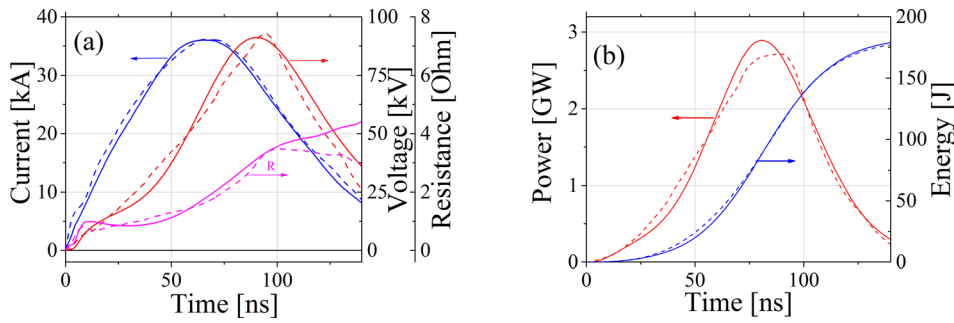


FIG. 5. (a) Waveforms of the current measured by the CVR, the resistive voltage, and the wire resistance. (b) The deposited power and the energy. Experiment (solid lines) and MHD simulation (dashed lines).

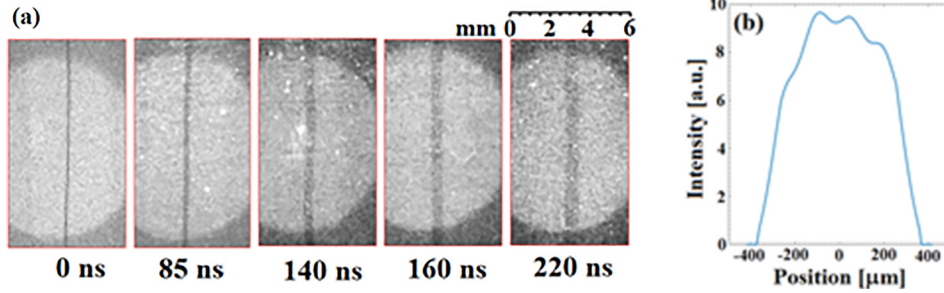


FIG. 6. (a) X-ray shadow images of an exploding Cu wire. (b) Profile of the x-ray image at  $t = 220$  ns. The time is measured between the beginning of the current and the peak in the x-ray intensity registered by the PMT.

temperatures is shown in Fig. 4. Here, let us note that the SESAME EOS<sup>11</sup> did not need to be modified in the temperature and density range realized in the present experiment. Input parameters for the simulations were the charging voltage and the parameters of the water forming line and the load.

#### IV. EXPERIMENTAL RESULTS AND ANALYSIS

Typical current and resistive voltage waveforms obtained for Cu wire explosions are shown in Fig. 5 together with the power, the energy deposition, and the evolution of the wire resistance. One can see that the main energy deposition occurs within 50–120 ns, resulting in a deposited energy density of  $\sim 50$  eV/atom ( $\sim 30$  kJ/g) and a maximal wire resistance of  $\sim 4$   $\Omega$ . In Fig. 5(a), the MHD simulated current and resistive voltage waveforms are in good agreement with the experimental values.<sup>12</sup>

Typical X-ray images of the wire prior to ( $t = 0$  ns) and during the wire explosion are shown in Fig. 6. One can distinctly determine the boundary of the expanded wire with an error of  $\pm 30$   $\mu\text{m}$  up to  $t = 240$  ns. The X-ray images do not show the formation of striations ( $> 30$   $\mu\text{m}$ ), typical for thermal instabilities obtained for wire explosions in vacuum.<sup>39</sup> The latter can be explained by significantly larger density of the exploding wire in water than in vacuum and consequently smaller increment of the thermal instability which is inversely proportional to the density. Also, these images show clear boundaries of the exploding wire without indications of pinch or hose type MHD instabilities.

Using these X-ray images, the radial expansion of the wire was determined up to a diameter of  $\sim 800$   $\mu\text{m}$  (at  $t = 240$  ns) and compared with the results of 1D MHD simulations, as shown in Fig. 7. There is satisfactory agreement between the experimentally obtained and simulated radial trajectories of the expanding wire with only very small differences at  $t > 200$  ns. This agreement indicates that the EOS

database used<sup>11</sup> is accurate for the density, internal energy, and temperature range realized in the present experiment. The average velocity of the wire expansion during the time when the main portion of the energy has been deposited (75–150 ns) was found to be  $\sim 2 \times 10^5$  cm/s, decreasing to  $\sim 1.7 \times 10^5$  cm/s later in time. These data agree with the earlier published results where laser backlighting streak images of exploding wires were used to estimate the radial expansion of the wire.<sup>27</sup> Here, let us note that at earlier times, backlighting can only be used as an estimate of the wire expansion, because the shock wave and wire radius expansions cannot be distinguished.

Using the inverse Abel transform, one can reconstruct an azimuthal symmetric function from line of sight integration measurements. The wire density  $\rho(r)$  is reconstructed using the projection of the X-rays onto the axis perpendicular to the wire.<sup>40</sup> For this analysis, the radial distribution of the density is the result of averaging along the 3–8 mm section of the X-ray image. Due to the low spatial resolution and

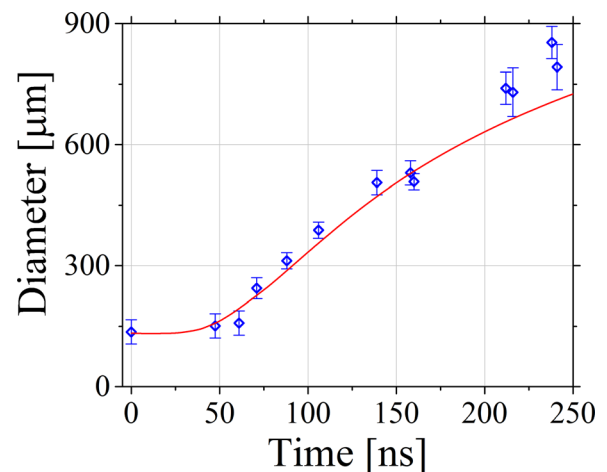


FIG. 7. Radial expansion of the exploding wire: dots—experiment and solid line—MHD simulation.

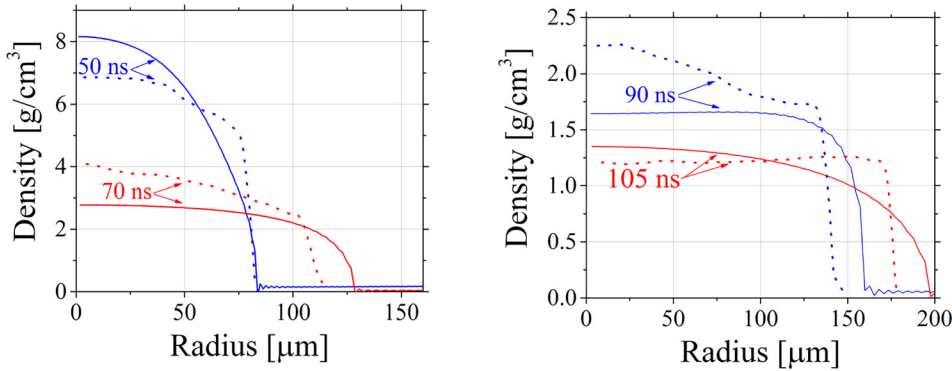


FIG. 8. Radial density distribution. Experiment (solid lines) and MHD simulation (dotted lines).

contrast, an 8th degree (symmetric) polynomial fit had to be used to fit the raw data to obtain reasonable results from the inversion process. However, this polynomial fit introduced artificial structures at the edges of the obtained images and smoothed out sharp deviations in the wire density. For better reconstruction, the image quality needs to be improved in the future. The reconstruction was performed using the Fourier-Hankel approach described in Ref. 41. The average error of the density values, using the results of the inverse Abel transform of a few wire parts of one X-ray image, was estimated to be  $\pm 10\%$ . Examples of radial density distributions obtained prior to the maximum of the discharge current and during the main part of energy deposition into the wire are shown in Fig. 8 together with the results of 1D MHD simulations. Here, the absolute values of the density were obtained using the mass conservation law, namely, the obtained density distribution  $g(r)$  was multiplied by the coefficient  $\alpha = r_0^2 \rho_0 / 2 \int_0^R g(r) r dr$ , where  $r_0 = 6.5 \times 10^{-3}$  cm and  $\rho_0 = 8.96$  g/cm<sup>3</sup> are the initial radius and density of the copper wire, respectively, and  $R$  is the radius of expanded wire at a given time. One can see that at  $t = 50$  ns, the value of the experimental density on axis is higher (by  $\sim 10\%$ ) than the simulated one. Later in the explosion, this behavior is reversed, i.e., simulated density on axis is larger than the experimental value, and the density becomes relatively uniform at later times. Only at  $t > 100$  ns, do the experimental and simulated radial density distributions become almost identical except at the periphery. Closer to the edge of the wire, the error of the inverse Abel transform analysis increases because of the polynomial fit and the high dynamic range for which the inversion method introduces artificial structures.

The obtained X-ray shadow images with a spatial resolution of  $50 \mu\text{m}$  of the exploding wire do not show thermal instabilities, i.e., striation typical to wire explosions in vacuum or gas. Such instabilities develop due to the unavoidable initial microscopic non-uniformity of the resistivity. This non-uniformity causes increased energy density deposition at the locations with larger resistivity leading to a further increase in resistivity and radial redistribution of the current to the nearby area where the resistivity is lower. This leads to the formation of a layer with increased temperature and pressure. The latter causes layer expansion and compression of the adjustment layer and consequently a decrease in its resistivity. Thus, one obtains hot low-density and cold high-

density layer formation. The increment of this instability is inversely proportional to the density of the material.<sup>39</sup> Thus, one can consider that for underwater explosions, due to significantly lower exploding wire radial expansion velocity, compared to gas or vacuum, the increment of this instability is rather small not allowing this instability to develop on a nanosecond timescale.

The radial density distribution obtained by the Abel transform method of X-ray images agrees with the MHD simulated distribution. This indicates that the changes introduced into the BKL conductivity model are correct.

## V. SUMMARY

Using a modified X-ray source based on the rod-ring vacuum electron diode, reliable and high-contrast x-ray images with  $\sim 30 \mu\text{m}$  space and  $\sim 10$  ns time resolution of ns-timescale underwater electrical explosion of copper wire were obtained. Applying an inverse Abel transform, the radial density distributions of the exploding wire to densities as low as  $\sim 1$  g/cm<sup>3</sup> were reconstructed, showing satisfactory fit with density distributions simulated using 1D MHD modeling with a modified conductivity model. The validity of this modification was confirmed by a satisfactory matching of the experimental and simulated current, voltage waveforms, and radial wire expansion. In addition, the X-ray images show the absence of MHD and thermal instabilities during ns-timescale copper wire underwater explosion.

## ACKNOWLEDGMENTS

We thank Dr. J. G. Leopold for his kind assistance in modelling the X-ray diode and critical reading of the manuscript. This research was supported by the Center for Absorption in Science, Ministry of Immigrant Absorption, State of Israel.

<sup>1</sup>A. W. DeSilva and J. D. Kunze, *Phys. Rev. E* **57**, 5945 (1997).

<sup>2</sup>N. I. Kuskova, S. I. Tkachenko, and S. V. Koval, *J. Phys.: Condens. Matter* **9**, 6175 (1997).

<sup>3</sup>W. DeSilva and J. D. Katsouras, *Phys. Rev. E* **57**, 5945 (1998).

<sup>4</sup>V. I. Oreshkin, R. B. Baksht, A. Yu. Labezkii, A. G. Roussikh, A. V. Shishlov, P. R. Levashov, K. V. Khishchenko, and I. V. Glazyrin, *Tech. Phys.* **49**, 843 (2004).

<sup>5</sup>A. E. Ter-Oganeyan, S. I. Tkachenko, V. M. Romanova, A. R. Mingaleev, T. A. Shelkovenko, and S. A. Pikuz, *Plasma Phys. Rep.* **31**, 919 (2005).

- <sup>6</sup>S. A. Pikuz, S. I. Tkachenko, V. M. Romanova, T. A. Shelkovenko, A. E. Ter-Oganessian, and A. R. Mingaleev, *IEEE Trans. Plasma Sci.* **34**, 2330 (2006).
- <sup>7</sup>A. G. Rousskikh, V. I. Oreshkin, A. Yu. Labetsky, S. A. Chaikovskiy, and A. V. Shishlov, *Techn. Phys.* **52**, 571 (2007).
- <sup>8</sup>K.-J. Chung, K. Lee, Y. S. Hwang, and D.-K. Kim, *J. Appl. Phys.* **120**, 203301 (2016).
- <sup>9</sup>Ya. E. Krasik, A. Grinenko, A. Sayapin, S. Efimov, A. Fedotov, V. Tz. Gurovich, and V. I. Oreshkin, *IEEE Trans. Plasma Sci.* **36**, 423 (2008) and references therein.
- <sup>10</sup>V. E. Fortov and I. T. Iakubov, *The Physics of Non-Ideal Plasma* (World Scientific, Singapore, 2000).
- <sup>11</sup>National Technical Information Service Document No. DE85014241 (S. P. Lyon and J. D. Johnson, "Sesame: The Los Alamos National Laboratory Equation-of-State Database," LANL Report No. LA UR-92-3407, 1992). Copies may be ordered from the National Technical Information Service, Springfield, VA, 22161.
- <sup>12</sup>Yu. D. Bakulin, V. F. Kuropatenko, and A. V. Luchinskii, *Sov. Phys. Tech. Phys.* **21**, 1144 (1976).
- <sup>13</sup>R. M. More, K. H. Warren, D. A. Young, and G. B. Zimmerman, *Phys. Fluids* **31**, 3059 (1988).
- <sup>14</sup>R. Redmer, *Phys. Rev. E* **59**, 1073 (1999).
- <sup>15</sup>M. P. Desjarlais, *Contrib. Plasma Phys.* **41**, 267 (2001).
- <sup>16</sup>M. P. Desjarlais, J. D. Kress, and L. A. Collins, *Phys. Rev. E* **66**, 025401 (R) (2002).
- <sup>17</sup>S. I. Tkachenko, K. V. Khishchenko, V. S. Vorob'ev, P. R. Levashov, I. V. Lomonosov, and V. E. Fortov, *High Temp.* **39**, 674 (2001).
- <sup>18</sup>S. I. Tkachenko, V. S. Vorob'ev, and S. P. Malysenko, *J. Phys. D: Appl. Phys.* **37**, 495 (2004).
- <sup>19</sup>A. Grinenko, Ya. E. Krasik, S. Efimov, A. Fedotov, V. Tz. Gurovich, and V. I. Oreshkin, *Phys. Plasmas* **13**, 042701 (2006).
- <sup>20</sup>D. Sheftman and Ya. E. Krasik, *Phys. Plasmas* **17**, 112702 (2010).
- <sup>21</sup>D. Sheftman and Ya. E. Krasik, *Phys. Plasmas* **18**, 092704 (2011).
- <sup>22</sup>D. Sheftman, D. Shafer, S. Efimov, and Ya. E. Krasik, *Phys. Plasmas* **19**, 034501 (2012).
- <sup>23</sup>S. A. Chaikovskiy, V. I. Oreshkin, I. M. Datsko, N. A. Labetskaya, and N. A. Ratakhin, *Phys. Plasmas* **21**, 042706 (2014).
- <sup>24</sup>J. Stephens, J. Dickens, and A. Neuber, *Phys. Rev. E* **89**, 053102 (2014).
- <sup>25</sup>A. Virozub, V. Tz. Gurovich, D. Yanuka, O. Antonov, and Ya. E. Krasik, *Phys. Plasmas* **23**, 092708 (2016).
- <sup>26</sup>Ya. E. Krasik, S. Efimov, D. Sheftman, A. Fedotov-Gefen, O. Antonov, D. Shafer, D. Yanuka, M. Nitishinskiy, M. Kozlov, L. Gilburd, G. Toker, S. Gleizer, E. Zvulun, V. Tz. Gurovich, D. Varentsov, and M. Rodionova, *IEEE Trans. Plasma Sci.* **44**, 412 (2016).
- <sup>27</sup>D. Yanuka, A. Rososhek, and Ya. E. Krasik, *Phys. Plasmas* **24**, 053512 (2017).
- <sup>28</sup>T. Sasaki, Y. Yano, M. Nakajima, T. Kawamura, and K. Horioka, *Nucl. Instrum. Methods Phys. Res. A* **577**, 313 (2007).
- <sup>29</sup>D. Varentsov, O. Antonov, A. Bakhmutova, C. W. Barnes, A. Bogdanov, C. R. Danly, S. Efimov, M. Endres, A. Fertman, A. A. Golubev, D. H. H. Hoffmann, B. Ionita, A. Kantsyrev, Y. E. Krasik, P. M. Lang, I. Lomonosov, F. G. Mariam, N. Markov, F. E. Merrill, V. B. Mintsev, D. Nikolaev, V. Panyushkin, M. Rodionova, M. Schanz, K. Schoenberg, A. Semennikov, L. Shestov, V. S. Skachkov, V. Turtikov, S. Udrea, O. Vasylyev, K. Weyrich, C. Wilde, and A. Zubareva, *Rev. Sci. Instrum.* **87**, 023303 (2016).
- <sup>30</sup>S. Bland, D. Yanuka, and A. Rososhek, private communication.
- <sup>31</sup>T. A. Shelkovenko, S. A. Pikuz, D. B. Sinars, K. M. Chandler, and D. A. Hammer, *IEEE Trans. Plasma Sci.* **30**, 567 (2002).
- <sup>32</sup>T. A. Shelkovenko, S. A. Pikuz, and D. A. Hammer, *Plasma Phys. Rep.* **42**, 226 (2016).
- <sup>33</sup>T. A. Shelkovenko, S. A. Pikuz, C. L. Hoyt, A. D. Cahill, L. Atoyan, D. A. Hammer, I. N. Tilikin, A. R. Mingaleev, V. M. Romanova, and A. V. Agafonov, *Phys. Plasmas* **23**, 103303 (2016).
- <sup>34</sup>D. Sheftman, D. Shafer, S. Efimov, K. Gruzinsky, S. Gleizer, and Ya. E. Krasik, *Rev. Sci. Instrum.* **83**, 103505 (2012).
- <sup>35</sup>M. Nitishinskiy, D. Yanuka, A. Virozub, and Ya. E. Krasik, *Phys. Plasmas* **24**, 122703 (2017).
- <sup>36</sup>A. Khacef, R. Viladrosa, C. Cachoncinlle, E. Robert, and J. M. Povesle, *Rev. Sci. Instrum.* **68**, 2292 (1997).
- <sup>37</sup>See <http://fieldp.com/trak.html> for information about the Trak Charged Particle Toolkit.
- <sup>38</sup>J. Punnoose, J. Xu, A. Sisniega, W. Zbijewski, and J. H. Siewerdsen, *Med. Phys.* **43**, 4711 (2016).
- <sup>39</sup>V. I. Oreshkin, *Phys. Plasmas* **15**, 092103 (2008).
- <sup>40</sup>H. R. Griem, *Principles of Plasma Spectroscopy* (Cambridge University Press, Cambridge, 1997).
- <sup>41</sup>L. M. Smith, D. R. Keefer, and S. I. Sudharsanan, *J. Quant. Spectrosc. Radiat. Transfer* **39**, 367 (1988).